Article

Vertically Stacked Amorphous Ir/Ru/Ir Oxide Nanosheets for Boosted Acidic Water Splitting

Junmin Li,[#] Geng Wu,[#] Zixiang Huang,[#] Xiao Han, Bei Wu, Peigen Liu, Haohui Hu, Ge Yu, and Xun Hong*

Cite This: JACS Au 2024, 4, 1243−1249

Read Online

ACCESS | Metrics & More | Article Recommendations | Supporting Information

ABSTRACT: Integrating multiple functional components into vertically stacked heterostructures offers a prospective approach to manipulating the physicochemical properties of materials. The synthesis of vertically stacked heterogeneous noble metal oxides remains a challenge. Herein, we report a surface segregation approach to create vertically stacked amorphous Ir/Ru/Ir oxide nanosheets (NSs). Cross-sectional high-angle annular darkfield scanning transmission electron microscopy images demonstrate a three-layer heterostructure in the amorphous Ir/Ru/Ir oxide NSs, with IrO$_x$ layers located on the upper and lower surfaces, and a layer of RuO$_x$ sandwiched between the two IrO$_x$ layers. The vertically stacked heterostructure is a result of the diffusion of Ir atoms from the amorphous IrRuO$_x$ solid solution to the surface. The obtained A-Ir/Ru/Ir oxide NSs display an ultralow overpotential of 191 mV at 10 mA cm^{-2} toward acid oxygen evolution reaction and demonstrate excellent performance in a proton exchange membrane water electrolyzer, which requires only 1.63 V to achieve 1 A cm^{-2} at 60 °C, with virtually no activity decay observed after a 1300 h test.

KEYWORDS: vertically stacked heterostructures, amorphous nanosheets, surface segregation, acidic water splitting, PEM water electrolyzer
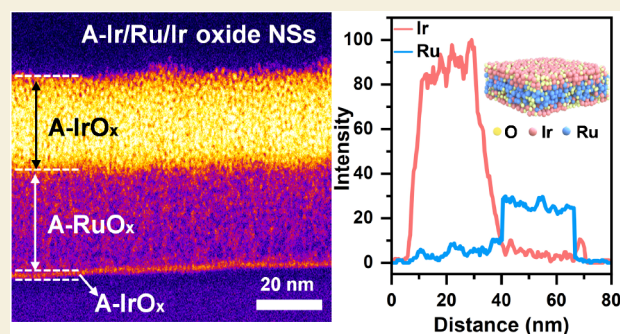
Anodic oxygen evolution reaction (OER) poses a critical bottleneck in the efficiency and durability of proton exchange membrane (PEM) electrolyzers.[1,2] The harsh acidic and oxidative environment restricts the practical application of most OER electrocatalysts, with only Ir-based oxides exhibiting necessary corrosion resistance.[3−6] Nevertheless, the scarcity and relatively low OER activity of Ir fall short of industrial demands.[7,8] Incorporating Ru in Ir-based oxides is an effective strategy to achieve both high activity and long-term stability.[9−12] For example, IrRuO$_x$ solid solution effectively modulates the electronic properties of active sites by the synergy between Ru and Ir, facilitating the adsorption of oxygen intermediates.[13−16] However, the IrRuO$_x$ solid solution inevitably undergoes Ir surface enrichment with partial active Ru species leaching under electrochemically induced restructuring,[17] which suggests that surface Ir enrichment is conducive to the stability enhancement of IrRu oxides and a better trade-off of the activity−stability relationship.

Two-dimensional (2D) vertically stacked heterostructures offer three- or multilayer structures with distinct interfaces, allowing diverse matching according to specific needs and showcasing remarkable tunability in surface-exposed atoms.[18−21] 2D vertically stacked heterostructures provide a favorable configuration for constructing an IrRu oxide with surfaces enriched Ir for the acidic OER. Mechanical stacking of exfoliated flakes and epitaxial growth are common methods for fabricating vertically stacked heterostructures.[22,23] However, mechanical stacking is suitable for constructing vertically stacked heterostructures in layered nanomaterials, but not for nonlayered noble metal oxides.[24−26] Moreover, achieving 2D vertically stacked heterostructures of noble metal oxides through epitaxial growth, in addition to strict restrictions on the crystallinity, lattice symmetry, and lattice constant of materials, precious control of nucleation and growth kinetics is also required to prevent island growth.[27,28] Alternatively, amorphous vertically stacked heterostructures, which are not bound by lattice matching, thus provide more flexibility in the integration of multiple functional components. Meanwhile, compared with the periodic atomic arrangement of crystalline structure, disordered atomic packing in amorphous nanostructure endows them with lower volume density and more vacancies as well as isotropic diffusion channels.[29,30] Additionally, atomic diffusion in amorphous structures shows lower activation energy[31−33] and higher diffusion rates[34,35] compared to its crystalline counterpart. These factors open up exciting
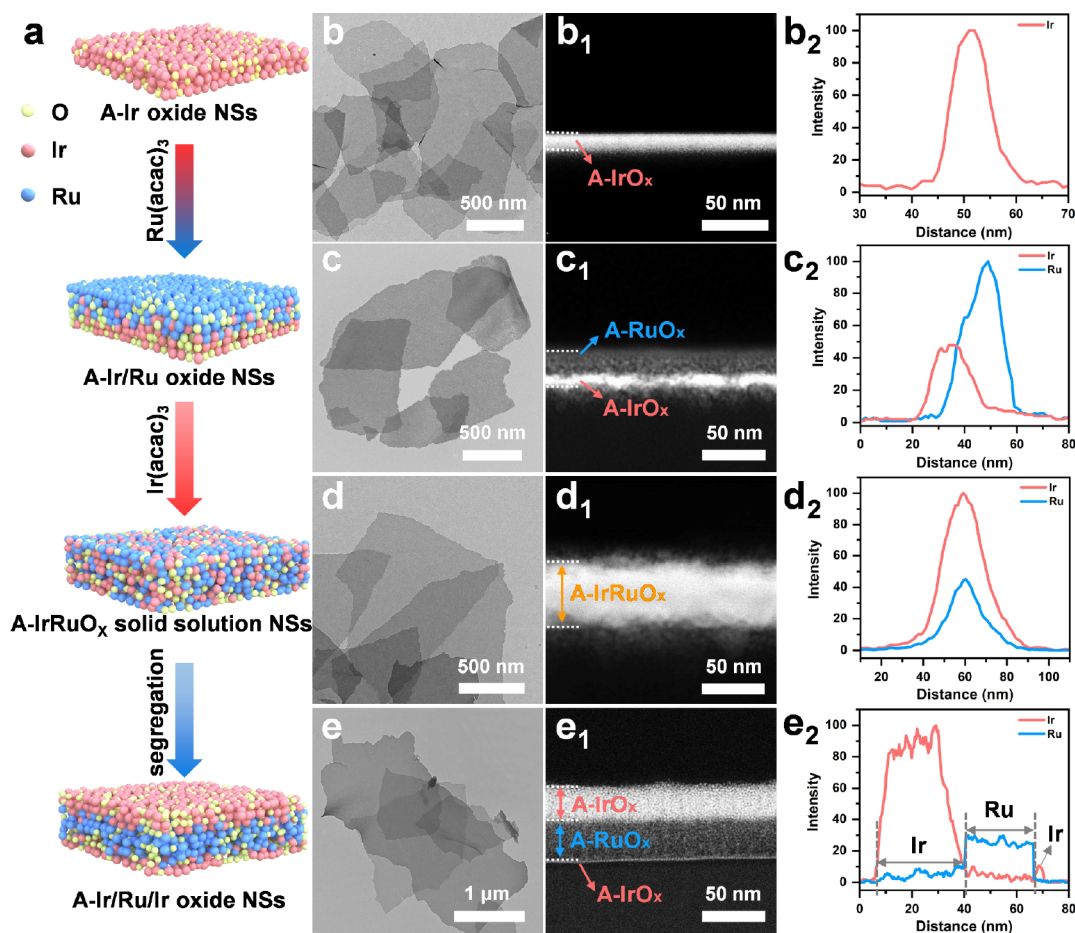
1243

Figure 1. (a) Schematic illustration of the synthesis process from A-Ir NSs to A-Ir/Ru/Ir oxide NSs. Note: the red balls represent Ir atoms, the blue balls represent Ru atoms, and yellow ones represent O atoms. (b−e) TEM images. (b_1, c_1, d_1, e_1) Cross-sectional HAADF-STEM images. (b_2, c_2, d_2, e_2) Corresponding cross-sectional EDS line profiles of A-Ir oxide NSs, A-Ir/Ru oxide NSs, A-IrRuO$_x$ solid solution NSs, and A-Ir/Ru/Ir oxide NSs, respectively.

prospects for creating vertically stacked heterostructures of noble metal oxides through atomic diffusion in amorphous nanomaterials.

Herein, we synthesized amorphous Ir/Ru/Ir oxide nanosheets (denoted as A-Ir/Ru/Ir oxide NSs) with a three-layer vertically stacked heterostructure through surface segregation. The synthesized A-Ir/Ru/Ir oxide NSs exhibit a 191 mV overpotential for achieving 10 mA cm^{-2} in acidic OER and sustained operation for 1300 h in a PEM water electrolyzer with negligible activity decay.
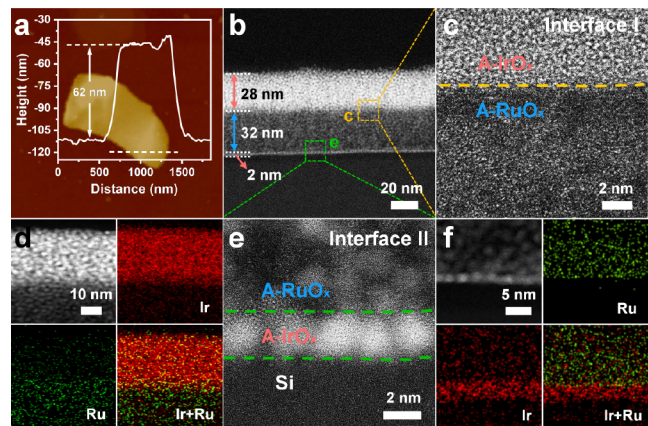
■ SYNTHESIS OF A-IR/RU/IR OXIDE NSS

Figures 1a and S1 illustrate the formation process of A-Ir/Ru/Ir oxide NSs. Amorphous Ir oxide nanosheets (A-Ir oxide NSs) were synthesized by annealing a mixture of Ir(acac)$_3$ and KNO$_3$ in air. Subsequently, Ru(acac)$_3$ is deposited on the A-Ir oxide NSs to obtain amorphous Ir/Ru oxide nanosheets (A–Ir/Ru oxide NSs). Finally, Ir(acac)$_3$ and A-Ir/Ru oxide NSs were calcined at 285 °C. An intermediate state, characterized by amorphous IrRuO$_x$ solid solution nanosheets (A-IrRuO$_x$ solid solution NSs), were captured through rapid cooling in liquid nitrogen to preserve structural characteristics at 285 °C, while A-Ir/Ru/Ir oxide NSs were obtained through natural cooling. The X-ray diffraction (XRD) pattern affirms their amorphous nature, as there are no discernible diffraction peaks (Figure S2). Transmission electron microscopy (TEM) image

(Figure 1b) and atomic force microscopy (AFM) image (Figure S3) reveal the micrometer-scale dimensions of A-Ir oxide NSs, with a thickness of 11 nm. Cross-sectional high-angle annular dark-field scanning transmission electron microscopy (HAADF-STEM) image (Figure 1b$_1$), corresponding energy dispersive X-ray spectroscopy (EDS) line profiles (Figures 1b$_2$ and S4a), and EDS elemental mappings (Figure S5) show homogeneous distribution of Ir throughout the A-Ir oxide NSs. For A-Ir/Ru oxide NSs, the TEM image (Figure 1c) and AFM image (Figure S6) clearly show an increase in its thickness to 35.5 nm. Cross-sectional HAADF-STEM image (Figure 1c$_1$) clearly reveals a two-layer vertical structure of A-Ir/Ru oxide NSs, featuring a pronounced contrast difference at the interface. Moreover, cross-sectional EDS line profiles (Figures 1c$_2$ and S4b) and EDS elemental mappings (Figure S7) confirm that the top dark layer corresponds to the RuO$_x$ layer, while the bottom bright layer corresponds to the IrO$_x$ layer. Meanwhile, the cross-sectional high-resolution transmission electron microscopy (HRTEM) image (Figure S8) clearly shows the vertical distribution trend of the Ir and Ru atoms at the interface. A-IrRuO$_x$ solid solution NSs, depicted in Figures 1d and S9, exhibit a micrometer size and a thickness of 51.8 nm. The random atomic arrangement of Ir and Ru depicted in the HRTEM image (Figure S10) indicates the amorphous structure of the A-IrRuO$_x$ solid solution NSs. Cross-sectional HAADF-STEM image (Figure 1d$_1$), corre-

sponding EDS line profiles (Figures 1d$_2$ and S4c) and EDS elemental mappings (Figure S11) indicate a uniform distribution of Ir and Ru atoms within the A-IrRuO$_x$ solid solution NSs. Figure 1e displays A-Ir/Ru/Ir oxide NSs, maintaining a micrometer-scale transverse dimension. Elemental mappings (Figure S12) indicate a homogeneous distribution of Ir, Ru, and O in the planar. Cross-sectional HAADF-STEM image (Figure 1e$_1$) and corresponding EDS line profiles (Figures 1e$_2$ and S4d) provide a clear visualization of the three-layer vertical heterostructure of A-Ir/Ru/Ir oxide NSs. Among them, the bright regions observed on the upper and lower surfaces correspond to the IrO$_x$ layer, while the middle section corresponds to the RuO$_x$ layer. This distinction is clearly discernible due to the contrast disparity between Ir and Ru. We propose that the transition from IrRuO$_x$ solid solution to the three-layer vertical structure of A-Ir/Ru/Ir oxide NSs results from the rearrangement of atoms induced by surface segregation of Ir atoms, driven by the difference in surface energy between Ir and Ru.[36,37]

To further investigate A-Ir/Ru/Ir oxide NSs, we conducted a detailed characterization. As shown in Figure 2a, the AFM

Figure 2. Characterization of A-Ir/Ru/Ir oxide NSs. (a) AFM image and (b) cross-sectional HAADF-STEM image of A-Ir/Ru/Ir oxide NSs. (c) Cross-sectional aberration-corrected HAADF-STEM image and (d) corresponding EDS elemental mapping of interface I in A-Ir/Ru/Ir oxide NSs. (e) Cross-sectional aberration-corrected HAADF-STEM image and (f) corresponding EDS elemental mapping of interface II in A-Ir/Ru/Ir oxide NSs.

image indicates a thickness of 62 nm for A-Ir/Ru/Ir oxide NSs. Figure 2b is an enlargement of Figure 1e$_1$, providing a clearer view of the vertical heterostructure of the A-Ir/Ru/Ir oxide NSs. The top IrO$_x$ layer is approximately 28 nm thick, the middle RuO$_x$ layer is about 32 nm thick, and the bottom IrO$_x$ layer is approximately 2 nm thick. Two distinct hetero-interfaces, labeled interfaces I and II, are formed between the surface IrO$_x$ layer and the intermediate RuO$_x$ layer. Cross-sectional aberration-corrected HAADF-STEM image (Figure 2c) reveals the disordered atomic arrangement of the IrO$_x$ and RuO$_x$ layers at interface I. EDS elemental mapping (Figure 2d) clearly illustrates the distribution region of Ir and Ru, confirming the locations of the IrO$_x$ layer and RuO$_x$ layer at interface I. Figure 2e,f demonstrates the disordered atomic arrangement and the distribution region of Ir and Ru at interface II, providing further compelling evidence for the amorphous three-layer vertical structure of A-Ir/Ru/Ir oxide NSs.

ATOMIC AND ELECTRONIC STRUCTURES OF A-IR/RU/IR OXIDE NSS

X-ray photoelectron spectroscopy (XPS) measurements were carried out to determine the oxidation state of the Ru and Ir species. As shown in Figure 3a, A-Ir/Ru/Ir oxide NSs demonstrate a 0.2 eV positive shift in the Ru(III) and Ru(IV) peaks compared to A-Ir/Ru oxide NSs,[38] confirming a higher valence state of Ru in A-Ir/Ru/Ir oxide NSs. Ir 4f XPS spectra (Figure 3b) of A-Ir/Ru/Ir oxide NSs be fitted with three pairs of peaks centered at 61.5 and 64.5 eV, 62.1 and 65.1 eV, and 63.2 and 66.2 eV, which can be attributed to Ir (0), Ir (III), and Ir (IV), respectively.[39,40] In comparison with A-Ir oxide NSs and A-Ir/Ru oxide NSs, the Ir 4f XPS spectra of A-Ir/Ru/Ir oxide NSs show a significant negative shift, suggesting that Ir in A-Ir/Ru/Ir oxide NSs possesses the lowest oxidation states.

X-ray absorption near-edge structure (XANES) spectra were employed to investigate the electron transition behavior and electronic structure. The normalized Ru K-edge of A-Ir/Ru oxide NSs and A-Ir/Ru/Ir oxide NSs shows a similar spectral shape and edge position to the reference RuO$_2$ (Figure 3c), which identified that the average valence state of Ru species in A-Ir/Ru oxide NSs and A-Ir/Ru/Ir oxide NSs is close to +4. A-Ir/Ru/Ir oxide NSs exhibit a slight positive shift compared to A-Ir/Ru oxide NSs, suggesting an increase in the Ru oxidation state. The Ir L$_3$-edge (Figure 3d) shows the average valence states of Ir in the order of IrO$_2$ > A-Ir/Ru oxide NSs > A-Ir oxide NSs > A-Ir/Ru/Ir oxide NSs > Ir foil. XANES results for the Ru K-edge and Ir L$_3$-edge reveal an increase in Ru valence and a decrease in Ir valence in A-Ir/Ru/Ir oxide NSs compared to A-Ir/Ru oxide NSs, consistent with the XPS results. The converse shift of Ru and Ir valence states within the A-Ir/Ru/Ir oxide NSs could be attributed to changes in the heterogeneous interface, which triggers the charge redistribution of Ir and Ru atoms on the vertically stacked heterointerfaces, with a transfer of electrons from Ru to Ir, and thus an increase in the Ru valence and a decrease in the Ir valence.[40] The Fourier transforms of the extended X-ray absorption fine structure (FT-EXAFS) spectra of A-Ir/Ru/Ir oxide NSs at the Ru K-edge (Figures 3e, S13, and Table S1) show a dominant peak at approximately 1.50 Å, corresponding to the Ru−O bond. According to the fitting results, the coordination numbers (CNs) of the Ru−O bond in A-Ir/Ru/Ir oxide are smaller than those in crystalline RuO$_2$, which is attributed to the rich unsaturated coordination properties of the amorphous nanostructure. The FT-EXAFS spectra of Ir in R-space (Figures 3f, S14, and Table S2) demonstrate that IrO$_x$ in A-Ir/Ru/Ir oxide NSs exhibit nearly identical Ir−O bond lengths and similar coordination numbers as crystalline IrO$_2$, revealing the typical coordination octahedra of IrO$_6$ in A-Ir/Ru/Ir oxide NSs. Moreover, the presence of Ru−Ir/Ir-Ru bonds in the Ru K-edge and Ir L$_3$-edge spectra indicate an interaction between Ru and Ir at the heterointerface of the A-Ir/Ru/Ir oxide NSs.[13] The interactions in Ir−Ru local structures can prevent the formation of more soluble Ru/Ir high-valent complexes.[14,41]

ELECTROCATALYTIC ACTIVITY OF A-IR/RU/IR OXIDE NSS TOWARD OER

OER performances for A-Ir/Ru/Ir oxide NSs, A-Ir/Ru oxide NSs, A-Ir oxide NSs, commercial IrO$_2$ (Figure S15), and commercial RuO$_2$ (Figure S16) were evaluated in O$_2$-saturated 0.1 M HClO$_4$ electrolyte. As shown in the linear sweep voltammetry (LSV) curves and corresponding Tafel slopes
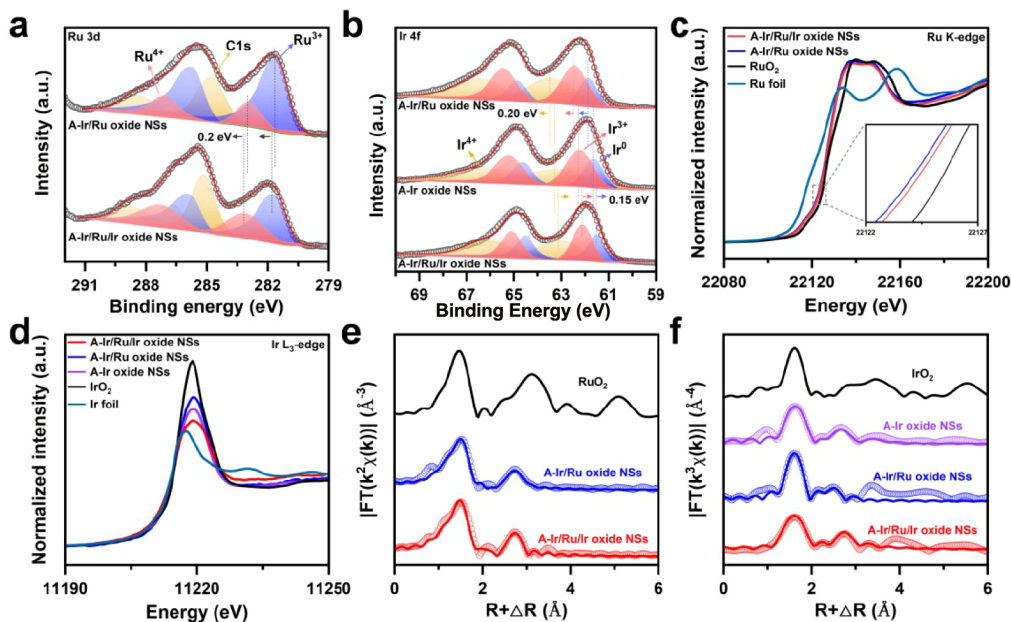
Figure 3. Spectroscopic studies of A-Ir oxide NSs, A-Ir/Ru oxide NSs, and A-Ir/Ru/Ir oxide NSs. (a) Ru $3d$ XPS spectra. (b) Ir $4f$ XPS spectra. (c) Ru K-edge XANES spectra. (d) Ir L_3-edge XANES spectra. (e) Fourier transforms of Ru K-edge EXAFS. (f) Fourier transforms of Ir L_3-edge EXAFS of A-Ir oxide NSs, A-Ir/Ru oxide NSs, and A-Ir/Ru/Ir oxide NSs, respectively.

(Figure 4a,b), the A-Ir/Ru/Ir oxide NSs show the best OER catalytic performance. The lowest overpotential was 191 mV at a current density of 10 mA cm^{-2} and a Tafel slope of 41.6 mV dec^{-1}, indicating that the A-Ir/Ru/Ir oxide NSs possess the fastest OER kinetics.

To compare the intrinsic catalytic activities of these catalysts, we calculated turnover frequency (TOF) at each noble metal site and mass activities according to the total loading mass of the noble metal (Table S3) in the catalysts. In Figure 4c, the TOF of A-Ir/Ru/Ir oxide NSs (0.855 s^{-1} at η = 300 mV) was about 4.4 and 4.5 times higher than that of A-Ir/Ru oxide NSs (0.194 s^{-1}) and A-Ir oxide NSs (0.192 s^{-1}), respectively. Additionally, the A-Ir/Ru/Ir oxide NSs reached the highest mass activity of 2377.1 A g$_{Ir+Ru}^{-1}$ at η = 300 mV (Figure 4d), which was nearly 17.5 and 69 times higher than that of commercial RuO$_2$ and commercial IrO$_2$, respectively. Furthermore, the A-Ir/Ru/Ir oxide NSs exhibit extremely high mass activity compared with previously reported noble metal electrocatalysts (Table S4). Apart from outstanding OER activity, A-Ir/Ru/Ir oxide NSs demonstrate excellent long-term stability, maintaining approximately 92% of current density over a 100 h chronoamperometry stability test, whereas A-Ir/Ru oxide NSs exhibit rapid decay after 22 h (Figure S17). We also employed ICP-MS to measure the dissolved amounts of Ru and Ir ions in the electrolyte at various intervals during the stability test of A-Ir/Ru/Ir oxide NSs (Figure S18). The exceedingly low concentration of Ru ions in the electrolyte indicates the effective protection of RuO$_x$ by the IrO$_x$ protective skeleton layer. Besides, the OER activity of A-Ir/Ru/Ir oxide NSs demonstrated minimal degradation even after 10,000 cycles (Figure S19), highlighting their outstanding stability. The results indicate that IrO$_x$ protective skeleton layer of A-Ir/Ru/Ir oxide NSs can significantly reduce the leaching of Ru and improve the stability of the catalyst. Meanwhile, as illustrated in Figure 4e, we systemically compared the OER performance of A-Ir/Ru/Ir oxide NSs and A-Ir/Ru oxide NSs, including overpotential, mass activity, Tafel slope, TOF, and

long-term stability. Compared to A-Ir/Ru oxide NSs, A-Ir/Ru/Ir oxide NSs demonstrate better performance in all of these metrics. The superior catalytic activity and overall performance of A-Ir/Ru/Ir oxide NSs surpass those of A-Ir/Ru oxide NSs, highlighting the significant performance advantage of the vertical heterostructure with RuO$_x$ sandwiched in the IrO$_x$ layer over the directly exposed RuO$_x$ surface, which underscores the importance of the vertical heterostructure with IrO$_x$-enriched surfaces for enhancing performance. Moreover, the Nyquist plots (Figure S20) show that the A-Ir/Ru/Ir oxide NSs have the lowest charge-transfer resistance among all of the tested catalysts, verifying the faster charge transfer process for A-Ir/Ru/Ir oxide NSs. To confirm the mechanism of the OER on A-Ir/Ru/Ir oxide NSs, *in situ* attenuated total reflection surface enhanced infrared absorption spectroscopy (ATR-SEIRAS) was employed. The *in situ* ATR-SEIRAS spectra for A-Ir/Ru/Ir oxide NSs at different working potentials (Figure 4f) reveal a distinct absorption peak at 1148 cm^{-1} attributed to the O−O stretching of surface adsorbed *OOH,[42,43] which is a characteristic intermediate of the adsorption evolution mechanism (AEM) pathway, indicating that A-Ir/Ru/Ir oxide NSs follow the AEM pathway.

We finally assembled a single cell using A-Ir/Ru/Ir oxide NSs as the anode to assess its performance in a real proton exchange membrane (PEM) electrolyzer device (Figure S21). The A-Ir/Ru/Ir oxide NS electrolyzer (at 60 °C) required only 1.63 V to reach a current density of 1.0 A cm^{-2} (Figure 4g), surpassing the performance of commercial RuO$_2$ (1.72 V) and IrO$_2$ (1.80 V), as well as outperforming other previously reported advanced Ir/Ru-based catalysts (Table S5). Impressively, no significant activity decay was observed during the 1300 h test at gradient increasing current density (Figure 4h). Specifically, the cell voltage remained stable (with a fluctuation within 20 mV) for 600 h at a current density of 1.0 A cm^{-2}, and the voltage fluctuations were small when the current density was increased to 2.0 and 3.0 A cm^{-2}. Additionally, the polarization curve indicates a slight increase in the cell voltage
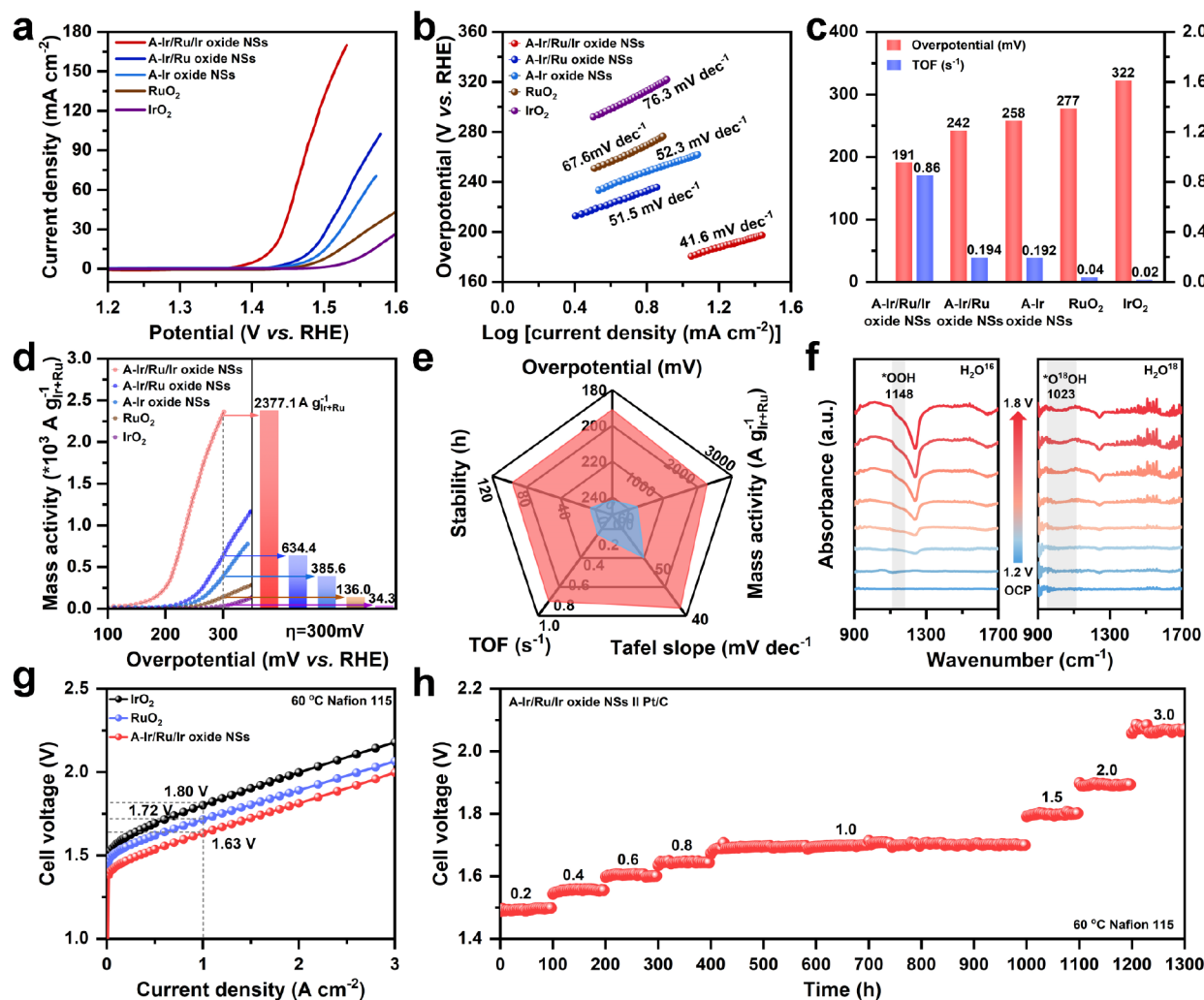
Figure 4. Electrochemical OER performance of A-Ir/Ru/Ir oxide NSs. (a) LSV curves. (b) Tafel plots. (c) Overpotential at 10 mA cm^{-2} (left axis) and TOF at η = 300 mV (right axis). (d) Mass activity of A-Ir/Ru/Ir oxide NSs, A-Ir/Ru oxide NSs, A-Ir oxide NSs, commercial RuO$_2$ and IrO$_2$, respectively. (e) Comparison of the OER performance between A-Ir/Ru/Ir oxide NS and A-Ir/Ru oxide NS. Light red represents A-Ir/Ru/Ir oxide NS, sky blue represents A-Ir/Ru oxide NS. (f) *In situ* ATR-SEIRAS of A-Ir/Ru/Ir oxide NSs at different potentials. (g) Polarization curves of the PEM electrolyzer using A-Ir/Ru/Ir oxide NSs as anodic catalysts coated on Nafion 115 membrane operated at 60 °C. (h) Chronopotentiometric curves of the PEM electrolyzer using A-Ir/Ru/Ir oxide NSs catalyst at a sequential current density of 0.2, 0.4, 0.6, 0.8, 1.0, 1.5, 2.0, and 3.0 A cm^{-2}.

after the 1300 h test (Figure S22). PEM electrolyzer test results demonstrate the good stability of the A-Ir/Ru/Ir oxide NSs and its excellent applicability under varying current densities. In addition, as shown in Figure S23, the TEM image and XRD pattern of A-Ir/Ru/Ir oxide NSs after the long-term durability test indicate negligible changes in morphology during the OER process, and the structural amorphous features remain unchanged.

In summary, we synthesized vertically stacked A−Ir−Ru-Ir oxide NSs. The prepared A-Ir/Ru/Ir oxide NSs exhibit a three-layer vertical heterostructure, with amorphous IrO$_x$ layers on the upper and lower surfaces, and a layer of amorphous RuO$_x$ sandwiched between the two IrO$_x$ layers. Impressively, the as-prepared A-Ir/Ru/Ir oxide NSs exhibit an ultralow over-potential (191 mV@10 mA cm^{-2}) and high mass activity (2377.1 A g$_{Ir+Ru}^{-1}$@300 mV) in acidic OER. The significant enhanced catalytic performance of A-Ir/Ru/Ir oxide NSs could be attributed to rich heterointerfaces, enabling substantially increased catalytically active sites and accelerated charge transfer kinetics. Additionally, A-Ir/Ru/Ir oxide NSs exhibited outstanding durability, sustaining performance for 1300 h in

the PEM electrolyzer with virtually no activity decay. Moreover, A-Ir/Ru/Ir oxide NSs exhibited stable operation even at high current densities of 2.0 and 3.0 A cm^{-2}. This work opens a new horizon for rationally exploiting surface segregation to deliberately synthesize and design electro-catalysts.

■ ASSOCIATED CONTENT

ⓢ Supporting Information

The Supporting Information is available free of charge at https://pubs.acs.org/doi/10.1021/jacsau.4c00085.

> Detailed experimental procedures, synthesis, physical characterizations, computational details, electrochemical measurements, and performance comparison (PDF)

■ AUTHOR INFORMATION

Corresponding Author

Xun Hong − *School of Chemistry and Materials Science, University of Science and Technology of China, Hefei*

230026, China; orcid.org/0000-0003-2784-2868;
Email: hongxun@ustc.edu.cn

Authors

Junmin Li − Center of Advanced Nanocatalysis (CAN), Department of Applied Chemistry, Hefei National Laboratory for Physical Sciences at the Microscale, University of Science and Technology of China, Hefei, Anhui 230026, China

Geng Wu − Center of Advanced Nanocatalysis (CAN), Department of Applied Chemistry, Hefei National Laboratory for Physical Sciences at the Microscale, University of Science and Technology of China, Hefei, Anhui 230026, China

Zixiang Huang − National Synchrotron Radiation Laboratory, University of Science and Technology of China, Hefei, Anhui 230029, China

Xiao Han − Center of Advanced Nanocatalysis (CAN), Department of Applied Chemistry, Hefei National Laboratory for Physical Sciences at the Microscale, University of Science and Technology of China, Hefei, Anhui 230026, China

Bei Wu − Center of Advanced Nanocatalysis (CAN), Department of Applied Chemistry, Hefei National Laboratory for Physical Sciences at the Microscale, University of Science and Technology of China, Hefei, Anhui 230026, China

Peigen Liu − National Synchrotron Radiation Laboratory, University of Science and Technology of China, Hefei, Anhui 230029, China

Haohui Hu − Center of Advanced Nanocatalysis (CAN), Department of Applied Chemistry, Hefei National Laboratory for Physical Sciences at the Microscale, University of Science and Technology of China, Hefei, Anhui 230026, China

Ge Yu − Center of Advanced Nanocatalysis (CAN), Department of Applied Chemistry, Hefei National Laboratory for Physical Sciences at the Microscale, University of Science and Technology of China, Hefei, Anhui 230026, China

Complete contact information is available at:
https://pubs.acs.org/10.1021/jacsau.4c00085

Author Contributions

[#]J.L., G.W., and Z.H. contributed equally to this work. All authors have given approval to the final version of the manuscript.

Notes

The authors declare no competing financial interest.

REFERENCES

(1) Xu, J.; Jin, H.; Lu, T.; Li, J.; Liu, Y.; Davey, K.; Zheng, Y.; Qiao, S.-Z. $IrO_x \cdot nH_2O$ with lattice water−assisted oxygen exchange for high-performance proton exchange membrane water electrolyzers. *Sci. Adv.* **2023**, *9* (25), No. eadh1718.

(2) Hao, Y.; Hung, S.-F.; Zeng, W.-J.; Wang, Y.; Zhang, C.; Kuo, C.-H.; Wang, L.; Zhao, S.; Zhang, Y.; Chen, H.-Y.; et al.etal. Switching the Oxygen Evolution Mechanism on Atomically Dispersed Ru for Enhanced Acidic Reaction Kinetics. *J. Am. Chem. Soc.* **2023**, *145* (43), 23659−23669.

(3) Zu, L.; Qian, X.; Zhao, S.; Liang, Q.; Chen, Y. E.; Liu, M.; Su, B.-J.; Wu, K.-H.; Qu, L.; Duan, L.; et al.etal. Self-Assembly of Ir-Based Nanosheets with Ordered Interlayer Space for Enhanced Electrocatalytic Water Oxidation. *J. Am. Chem. Soc.* **2022**, *144* (5), 2208−2217.

(4) Wu, G.; Zheng, X.; Cui, P.; Jiang, H.; Wang, X.; Qu, Y.; Chen, W.; Lin, Y.; Li, H.; Han, X.; et al.et al. A general synthesis approach for amorphous noble metal nanosheets. *Nat. Commun.* **2019**, *10*, 4855.

(5) Jin, H.; Liu, X.; An, P.; Tang, C.; Yu, H.; Zhang, Q.; Peng, H.-J.; Gu, L.; Zheng, Y.; Song, T.; et al.etal. Dynamic rhenium dopant boosts ruthenium oxide for durable oxygen evolution. *Nat. Commun.* **2023**, *14*, 354.

(6) Fan, R.-Y.; Zhang, Y.-S.; Lv, J.-Y.; Han, G.-Q.; Chai, Y.-M.; Dong, B. The Promising Seesaw Relationship Between Activity and Stability of Ru-Based Electrocatalysts for Acid Oxygen Evolution and Proton Exchange Membrane Water Electrolysis. *Small* **2023**, *20*, 2304636.

(7) Danilovic, N.; Subbaraman, R.; Chang, K. C.; Chang, S. H.; Kang, Y. J.; Snyder, J.; Paulikas, A. P.; Strmcnik, D.; Kim, Y. T.; Myers, D.; et al.etal. Activity−Stability Trends for the Oxygen Evolution Reaction on Monometallic Oxides in Acidic Environments. *J. Phys. Chem. Lett.* **2014**, *5* (14), 2474−2478.

(8) Wohlfahrt-Mehrens, M.; Heitbaum, J. Oxygen evolution on Ru and RuO_2 electrodes studied using isotope labelling and on-line mass spectrometry. *J. Electroanal. Chem. Interface Electrochem.* **1987**, *237* (2), 251−260.

(9) Kötz, R.; Stucki, S. Stabilization of RuO_2 by IrO_2 for anodic oxygen evolution in acid media. *Electrochim. Acta* **1986**, *31* (10), 1311−1316.

(10) Danilovic, N.; Subbaraman, R.; Chang, K. C.; Chang, S. H.; Kang, Y.; Snyder, J.; Paulikas, A. P.; Strmcnik, D.; Kim, Y. T.; Myers, D.; et al.etal. Using Surface Segregation To Design Stable Ru-Ir Oxides for the Oxygen Evolution Reaction in Acidic Environments. *Angew. Chem., Int. Ed.* **2014**, *53* (51), 14016−14021.

(11) Xia, T.; Liu, C.; Lu, Y.; Jiang, W.; Li, H.; Ma, Y.; Wu, Y.; Che, G. Regulating Ru-based double perovskite against lattice oxygen oxidation by incorporating Ir for efficient and stable acidic oxygen evolution reaction. *Appl. Surf. Sci.* **2022**, *605*, 154727.

(12) Wang, L.; Saveleva, V. A.; Zafeiratos, S.; Savinova, E. R.; Lettenmeier, P.; Gazdzicki, P.; Gago, A. S.; Friedrich, K. A. Highly active anode electrocatalysts derived from electrochemical leaching of Ru from metallic $Ir_{0.7}Ru_{0.3}$ for proton exchange membrane electrolyzers. *Nano Energy* **2017**, *34*, 385−391.

(13) Wen, Y.; Chen, P.; Wang, L.; Li, S.; Wang, Z.; Abed, J.; Mao, X.; Min, Y.; Dinh, C. T.; Luna, P. D.; et al.etal. Stabilizing Highly Active Ru Sites by Suppressing Lattice Oxygen Participation in Acidic Water Oxidation. *J. Am. Chem. Soc.* **2021**, *143* (17), 6482−6490.

(14) Zhu, W.; Song, X.; Liao, F.; Huang, H.; Shao, Q.; Feng, K.; Zhou, Y.; Ma, M.; Wu, J.; Yang, H.; et al.etal. Stable and oxidative charged Ru enhance the acidic oxygen evolution reaction activity in two-dimensional ruthenium-iridium oxide. *Nat. Commun.* **2023**, *14*, 5365.

(15) Zhuang, Z.; Wang, Y.; Xu, C.-Q.; Liu, S.; Chen, C.; Peng, Q.; Zhuang, Z.; Xiao, H.; Pan, Y.; Lu, S.; et al.etal. Three-dimensional

open nano-netcage electrocatalysts for efficient pH-universal overall water splitting. *Nat. Commun.* **2019**, *10*, 4875.

(16) Liu, S.; Tan, H.; Huang, Y.-C.; Zhang, Q.; Lin, H.; Li, L.; Hu, Z.; Huang, W.-H.; Pao, C.-W.; Lee, J.-F.; et al.et al. Structurally-Distorted RuIr-Based Nanoframes for Long-Duration Oxygen Evolution Catalysis. *Adv. Mater.* **2023**, *35* (42), 2305659.

(17) Escalera-López, D.; Czioska, S.; Geppert, J.; Boubnov, A.; Röse, P.; Saraçi, E.; Krewer, U.; Grunwaldt, J.-D.; Cherevko, S. Phase- and Surface Composition-Dependent Electrochemical Stability of Ir-Ru Nanoparticles during Oxygen Evolution Reaction. *ACS Catal.* **2021**, *11* (15), 9300−9316.

(18) Liu, X.; Gao, M.; Yang, H.; Zhong, X.; Yu, Y. 2D sandwich-like nanosheets of ultrafine Sb nanoparticles anchored to graphene for high-efficiency sodium storage. *Nano Res.* **2017**, *10* (12), 4360−4367.

(19) Sun, J.; Yang, D.; Lowe, S.; Zhang, L.; Wang, Y.; Zhao, S.; Liu, P.; Wang, Y.; Tang, Z.; Zhao, H.; et al.et al. Sandwich-Like Reduced Graphene Oxide/Carbon Black/Amorphous Cobalt Borate Nano-composites as Bifunctional Cathode Electrocatalyst in Rechargeable Zinc-Air Batteries. *Adv. Energy Mater.* **2018**, *8* (27), 1801495.

(20) Saleem, F.; Zhang, Z.; Cui, X.; Gong, Y.; Chen, B.; Lai, Z.; Yun, Q.; Gu, L.; Zhang, H. Elemental Segregation in Multimetallic Core−Shell Nanoplates. *J. Am. Chem. Soc.* **2019**, *141* (37), 14496−14500.

(21) Wang, Y.; Song, J.; Wong, W.-Y. Constructing 2D Sandwich-like MOF/MXene Heterostructures for Durable and Fast Aqueous Zinc-Ion Batteries. *Angew. Chem., Int. Ed.* **2023**, *135* (8), No. e202218343.

(22) Zhou, Z.; Hou, F.; Huang, X.; Wang, G.; Fu, Z.; Liu, W.; Yuan, G.; Xi, X.; Xu, J.; Lin, J.; et al.et al. Stack growth of wafer-scale van der Waals superconductor heterostructures. *Nature* **2023**, *621* (7979), 499−505.

(23) Lin, Z.; Yin, A.; Mao, J.; Xia, Y.; Kempf, N.; He, Q.; Wang, Y.; Chen, C.-Y.; Zhang, Y.; Ozolins, V.; et al.et al. Scalable solution-phase epitaxial growth of symmetry-mismatched heterostructures on two-dimensional crystal soft template. *Sci. Adv.* **2016**, *2* (10), No. e1600993.

(24) Kang, K.; Lee, K.-H.; Han, Y.; Gao, H.; Xie, S.; Muller, D. A.; Park, J. Layer-by-layer assembly of two-dimensional materials into wafer-scale heterostructures. *Nature* **2017**, *550*, 229−233.

(25) Lotsch, B. V. Vertical 2D Heterostructures. *Annu. Rev. Mater. Res.* **2015**, *45* (1), 85−109.

(26) Chen, Y.; Lai, Z.; Zhang, X.; Fan, Z.; He, Q.; Tan, C.; Zhang, H. Phase engineering of nanomaterials. *Nat. Rev. Chem.* **2020**, *4* (5), 243−256.

(27) Lu, Q.; Wang, A.-L.; Gong, Y.; Hao, W.; Cheng, H.; Chen, J.; Li, B.; Yang, N.; Niu, W.; Wang, J.; et al.et al. Crystal phase-based epitaxial growth of hybrid noble metal nanostructures on 4H/fcc Au nanowires. *Nat. Chem.* **2018**, *10* (4), 456−461.

(28) Liu, Y.; Huang, Y.; Duan, X. Van der Waals integration before and beyond two-dimensional materials. *Nature* **2019**, *567*, 323−333.

(29) Deng, S.; Yuan, Z.; Tie, Z.; Wang, C.; Song, L.; Niu, Z. Electrochemically Induced Metal−Organic-Framework-Derived Amorphous V 2 O 5 for Superior Rate Aqueous Zinc-Ion Batteries. *Angew. Chem., Int. Ed.* **2020**, *59* (49), 22002−22006.

(30) Wei, Z.; Wang, D.; Yang, X.; Wang, C.; Chen, G.; Du, F. From Crystalline to Amorphous: An Effective Avenue to Engineer High-Performance Electrode Materials for Sodium-Ion Batteries. *Adv. Mater. Interface* **2018**, *5* (19), 1800639.

(31) Strauß, F.; Dörrer, L.; Geue, T.; Stahn, J.; Koutsioubas, A.; Mattauch, S.; Schmidt, H. Self-Diffusion in Amorphous Silicon. *Phys. Rev. Lett.* **2016**, *116* (2), 025901.

(32) Zhang, W.; Huang, J.; Yu, X.; Liu, G.; Yanqin, H.; Fan, D. Atomic-level diffusion at the amorphous $Zr_{50}Cu_{50}$/crystalline Cu interface: A molecular dynamics study. *J. Adv. Join. Process.* **2022**, *6*, 100120.

(33) Posselt, M.; Bracht, H.; Ghorbani-Asl, M.; Radić, D. Atomic mechanisms of self-diffusion in amorphous silicon. *AIP Adv.* **2022**, *12* (11), 115325.

(34) Annamareddy, A.; Voyles, P. M.; Perepezko, J.; Morgan, D. Mechanisms of bulk and surface diffusion in metallic glasses

determined from molecular dynamics simulations. *Acta Mater.* **2021**, *209*, 116794.

(35) Wang, Y.-J.; Du, J.-P.; Shinzato, S.; Dai, L.-H.; Ogata, S. A free energy landscape perspective on the nature of collective diffusion in amorphous solids. *Acta Mater.* **2018**, *157*, 165−173.

(36) Ruban, A. V.; Skriver, H. L.; Nørskov, J. K. Surface segregation energies in transition-metal alloys. *Phys. Rev. B* **1999**, *59* (24), 15990−16000.

(37) Farsi, L.; Deskins, N. A. First principles analysis of surface dependent segregation in bimetallic alloys. *Phys. Chem. Chem. Phys.* **2019**, *21* (42), 23626−23637.

(38) Cao, D.; Wang, J.; Xu, H.; Cheng, D. Growth of Highly Active Amorphous RuCu Nanosheets on Cu Nanotubes for the Hydrogen Evolution Reaction in Wide pH Values. *Small* **2020**, *16* (37), 2000924.

(39) He, J.; Zhou, X.; Xu, P.; Sun, J. Regulating Electron Redistribution of Intermetallic Iridium Oxide by Incorporating Ru for Efficient Acidic Water Oxidation. *Adv. Energy Mater.* **2021**, *11* (48), 2102883.

(40) Shan, J.; Guo, C.; Zhu, Y.; Chen, S.; Song, L.; Jaroniec, M.; Zheng, Y.; Qiao, S.-Z. Charge-Redistribution-Enhanced Nanocrystal-line Ru@IrO_x Electrocatalysts for Oxygen Evolution in Acidic Media. *Chem* **2019**, *5* (2), 445−459.

(41) Escudero-Escribano, M.; Pedersen, A. F.; Paoli, E. A.; Frydendal, R.; Friebel, D.; Malacrida, P.; Rossmeisl, J.; Stephens, I. E. L.; Chorkendorff, I. Importance of Surface IrO_x in Stabilizing RuO_2 for Oxygen Evolution. *J. Phys. Chem. B* **2018**, *122* (2), 947−955.

(42) Du, K.; Zhang, L.; Shan, J.; Guo, J.; Mao, J.; Yang, C.-C.; Wang, C.-H.; Hu, Z.; Ling, T. Interface engineering breaks both stability and activity limits of RuO_2 for sustainable water oxidation. *Nat. Commun.* **2022**, *13*, 5448.

(43) Lang, C.; Li, J.; Yang, K. R.; Wang, Y.; He, D.; Thorne, J. E.; Croslow, S.; Dong, Q.; Zhao, Y.; Prostko, G.; et al.et al. Observation of a potential-dependent switch of water-oxidation mechanism on Co-oxide-based catalysts. *Chem* **2021**, *7* (8), 2101−2117.